



Brain dynamics and structure-function relationships via spectral factorization and the transfer function

James A. Henderson^{a,b,*}, Mukesh Dhamala^{c,d}, Peter A. Robinson^{a,b}

^a School of Physics, University of Sydney, New South Wales 2006, Australia

^b ARC Center for Integrative Brain Function, University of Sydney, New South Wales 2006, Australia

^c Department of Physics and Astronomy, Neuroscience Institute, Georgia State University, Atlanta, Georgia 30303, USA

^d Center for Behavioral Neuroscience, Center for Nano-Optics, and Center for Diagnostics and Therapeutics, Georgia State University, Atlanta, Georgia 30303, USA

A B S T R A C T

It is shown how the brain's linear transfer function provides a means to systematically analyze brain connectivity and dynamics, and to infer connectivity, eigenmodes, and activity measures such as spectra, evoked responses, coherence, and causality, all of which are widely used in brain monitoring. In particular, the Wilson spectral factorization algorithm is outlined and used to efficiently obtain linear transfer functions from experimental two-point correlation functions. The algorithm is tested on a series of brain-like structures of increasing complexity which include time delays, asymmetry, two-dimensionality, and complex network connectivity. These tests are used to verify the algorithm is suitable for application to brain dynamics, specify sampling requirements for experimental time series, and to verify that its runtime is short enough to obtain accurate results for systems of similar size to current experiments. The results can equally well be applied to inference of the transfer function in complex linear systems other than brains.

1. Introduction

The relationships between brain activity and structure are of central importance to understanding how the brain carries out its functions and to interrelating and predicting different kinds of experimental measurements. Several important characteristics of this structure-function relationship have been established. Firstly, mesoscale brain activity is approximately linear under normal conditions; experimental modalities like EEG and fMRI measure perturbations from mean levels of activity and are also approximately linear in these perturbations (Nunez, 1995; Robinson, 2012; Robinson et al., 2016). This is notwithstanding the fact that the dynamics of neurons and their substructures are highly nonlinear because linearity with respect to perturbations arises via averaging over large numbers of neurons (Robinson et al., 2002; 1997). Secondly, it has been increasingly recognized that if activity is to be correctly related to structure, temporal delays must be included in order to account for dynamics and causality, as a precursor to understanding signal processing in the brain (Babaie-Janvier and Robinson, 2018). Thirdly, mesoscale anatomical connectivity is approximately symmetric, with connections between pairs of points in both directions, but with some asymmetry; e.g., in the cortex, sensorimotor areas tend to project more strongly to frontal areas than vice versa, indicating a flow of signals during processing (Henderson and Robinson, 2014; Markov et al., 2012; Scannell et al., 1995). This work addresses the problem of how to systematically describe these characteristics of the brain and relate them to existing analyses, and how to obtain these characteristics from data.

The transfer function of a system contains complete information about its linear properties, responses, and dynamics. This includes relationships to impulse responses, spectra, and correlations. In the case of brain dynamics, it has been shown that the transfer function is closely related to brain connectivity, including time delays (Friston et al., 2014; Mehta-Pandjee et al., 2017; Robinson, 2012; 2019; Robinson et al., 2014; 2016), and we note that linear coupling is widely used to model the spatial interactions of locally nonlinear dynamics (Breakspear et al., 2010). Additionally, the eigenfunctions of the transfer function are natural modes of the system dynamics and thus underlie all spatial patterns of excitation in the cortex. Hence, the transfer function is well suited to describing and analyzing structure-function relationships in the brain.

The transfer function is equivalent to the Green function, or propagator, of the system (Robinson, 2012; 2019) and is thus given by the response $T(\mathbf{r}, t, \mathbf{r}_0, t_0)$ at position \mathbf{r} and time t , to a delta function input at \mathbf{r}_0 and t_0 . If the structure of the system is static, the value of t_0 is immaterial; however, direct measurement of T would involve stimulating at each point \mathbf{r}_0 and measuring the response at all other points \mathbf{r} and later times t — a task of order M^2 for an M -point discretization, with the additional complication that it is difficult, or impossible to stimulate every part of the cortex, for example, with equal intensity and a spatiotemporal delta function input.

Assumption of uniform white noise inputs has been shown to provide a good approximation to the electroencephalographic (EEG) spectrum over nearly three decades, a finding that has been tested in cohorts of

* Corresponding author.

E-mail addresses: james.henderson@sydney.edu.au (J.A. Henderson), mdhamala@gsu.edu (M. Dhamala), peter.robinson@sydney.edu.au (P.A. Robinson).

up to 2100 subjects (Abey Suriya et al., 2014; Abey Suriya and Robinson, 2016; Robinson et al., 2002; van Albada et al., 2007, 2010). A number of authors have since shown that it is possible to infer the transfer function from observed activity correlations if the spectrum of inputs is known, or if the white-noise approximation can be made (Friston et al., 2014; Mehta-Pandjee et al., 2017; Robinson, 2012; Robinson et al., 2014). These results reduce the problem to order M but have generally only been applicable to symmetric connectivities for which $T(\mathbf{r}, t, \mathbf{r}_0, t_0) = T(\mathbf{r}_0, t, \mathbf{r}, t_0)$. One exception was the work in MacLaurin and Robinson (2019), which applied the methods of Ephremidze et al. (2008) to factorize the spatially discretized correlation function into the product of the transfer function and its Hermitian conjugate, which are not equal in general. Broadly, the algorithm of T. Wilson (1972) has a shorter runtime than Ephremidze et al. (2008), but has comparable error for a well-behaved spectral matrix. The spectral factorization method of T. Wilson (1972) has been used to obtain Granger causality (Dhamala et al., 2008a,b), with the transfer function being an intermediate byproduct that was not studied in its own right.

The aim of this work is to describe the transfer function and its relationships to many existing forms of brain analysis. Then, to describe methods for obtaining the transfer function, with emphasis on spectral factorization using the Wilson algorithm (Dhamala et al., 2008; T. Wilson, 1972) applied to correlations of time series measurements. Criteria for time series sampling frequencies and durations are described for the algorithm to accurately estimate the transfer function. The algorithm is applied to a series of examples of increasing complexity and similarity to real brain structure in order to test and verify that it is free of numerical errors and instabilities (and modifying the method where required to ensure this), robust, and able to infer realistic structures from correlation functions, including asymmetry, time delays and complex network connectivity. The algorithm's runtime is verified to be such that it can feasibly be applied to systems composed of hundreds of points as in high spatial resolution experimental modalities, and is thus relevant for connection matrices containing up to 10^6 entries or more.

In this work we focus on the step of estimating the transfer function assuming a clean cross spectral density matrix of the system dynamics has been obtained. Application of spectral factorization to experimental data and interpretation of the resulting transfer function requires domain-specific analysis of the noise components, biases and artefacts, and sampling characteristics of the measurement modality used. For this reason we leave applications to data and detailed analysis of the impacts of noise, artefacts and biases for future work.

In Section 2 we outline the theory of the transfer function and its relationship to measures of brain function in continuous notation suitable for describing the brain which is continuous at the mesoscale, as well as in discretized notation that is suitable for describing experimental data that are inherently discretized measurements of the underlying continuous brain. Then, in Section 3.1, methods for determining the transfer function are explained, with emphasis on spectral factorization. Section IV discusses sampling criteria required in order to obtain accurate results. Section V is then devoted to demonstrating and testing the spectral factorization method on increasingly realistic and complicated structures using neural field theory (Robinson et al., 1997), introducing time delays, asymmetry, two-dimensionality, and complex network connectivity based on diffusion MRI (dMRI) data to verify the algorithm is suitable for application to brain dynamics.

2. Methods

In this section we define the transfer function and summarize how it relates to a range of structural and functional measures to illustrate its importance. This material is distilled from the references cited and is included here as essential background theory and to bring this material together for application in later sections.

2.1. Transfer function

Let us suppose that the quantity $Q_a(\mathbf{r}, t)$ represents the linear perturbation from the mean of the mean firing rate of neural population a at position \mathbf{r} and time t . Activity in population a is elicited by inputs from various afferent populations b , as well as direct external input N_a and we write (Robinson, 2019)

$$Q_a(\mathbf{r}, t) = \sum_b \int \int \Lambda_{ab}(\mathbf{r}, t, \mathbf{r}', t') Q_b(\mathbf{r}', t') d\mathbf{r}' dt' + N_a(\mathbf{r}, t), \quad (1)$$

where the causal propagator Λ_{ab} quantifies the direct effect of incoming activity to population a from population b and satisfies the causality condition

$$\Lambda_{ab}(\mathbf{r}, t, \mathbf{r}', t') = 0, \quad (2)$$

for $t < t'$; it corresponds to the system's bare propagator (Robinson, 2012). Alternatively, still in this linear regime, one can write

$$Q_a(\mathbf{r}, t) = \sum_b \int \int T_{ab}(\mathbf{r}, t, \mathbf{r}', t') N_b(\mathbf{r}', t') d\mathbf{r}' dt', \quad (3)$$

where T_{ab} is the transfer function from inputs to activity, which also satisfies causality. Because T_{ab} links all populations and locations, it represents the total effect of an activity perturbation in one population and a given location on another population at a different location, including all possible direct and indirect routes by which its influence can travel; it thus corresponds to the system's total propagator or Green function (Robinson, 2012).

At our scales of interest, the brain is continuous; however, experimental observations are inherently discrete, so it is useful to approximate the above description by discretizing and writing in discrete notation. We emphasize that this does not imply that the underlying system of the brain is discrete at the mesoscale.

If we discretize the continuous system described by Eqs (1) and (3) onto a spatial grid of M points, labeled \mathbf{r}_j with $j = 1, \dots, M$, we can rewrite them in a matrix form in which the activity and inputs become vectors containing the values at the discretized points, while $\Lambda_{ab}(\mathbf{r}, t, \mathbf{r}', t')$ and $T_{ab}(\mathbf{r}, t, \mathbf{r}', t')$ are represented by the elements of $M \times M$ matrices $\Lambda_{ab}(t, t')$ and $T_{ab}(t, t')$ (Robinson, 2019). If there are P populations of neurons, it is further possible to expand the dimensions of these quantities from M to MP and omit the subscripts ab , with the first M elements of each vector relating to population 1, the next M to population 2, and so forth, with corresponding blocks in multipopulation connectivities Λ and T .

This discretization of the spatial coordinate into points \mathbf{r}_j approximates integrals over space by summations, which themselves are described by the summations implicit in matrix multiplication

$$\int \Lambda_{ab}(\mathbf{r}_i, t, \mathbf{r}', t') Q_b(\mathbf{r}', t') d\mathbf{r}' \approx \sum_j \Lambda_{ij}(t, t') |\Delta \mathbf{r}'_j| Q_j(t'), \quad (4)$$

$$= \Lambda(t, t') Q(t'). \quad (5)$$

In Eq. (4) it is essential to note that the matrix elements in $\Lambda(t, t')$ represent $\Lambda_{ij}(t, t') |\Delta \mathbf{r}'_j|$, for example, where $|\Delta \mathbf{r}'_j|$ is the size of the region represented by the grid point that represents \mathbf{r}_j within its population; otherwise the dimensions of the above equations would not be compatible (Robinson, 2019). Incorporating the volume element into the description of the system is essential, but often overlooked in neuroscience leading to widespread flaws in analysis and interpretation of results (Robinson, 2019). For simplicity we assume that all the $|\Delta \mathbf{r}'_j|$ have a common value $|\Delta \mathbf{r}'|$ from now on.

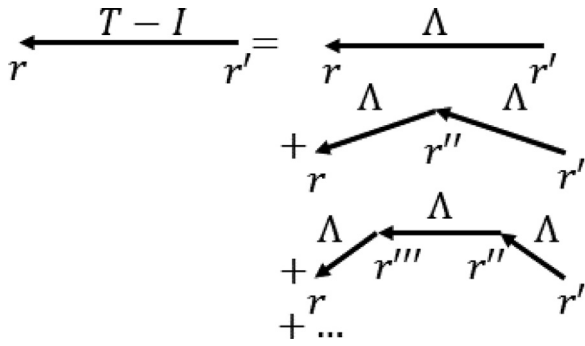


Fig. 1. Diagram of terms in the series expansion of $T(\omega)$ in Eq. (15), from point r' to r .

Thus in matrix notation one has

$$Q(t) = \int \Lambda(t, t')Q(t')dt' + N(t), \quad (6)$$

$$Q(t) = \int T(t, t')N(t')dt'. \quad (7)$$

Equations (6) and (7) can be written as convolutions if the structure is static and $\Lambda(t, t')$ and $T(t, t')$ depend only on $t - t'$, giving

$$Q(t) = \int \Lambda(t - t')Q(t')dt' + N(t), \quad (8)$$

$$Q(t) = \int T(t - t')N(t')dt'. \quad (9)$$

Upon Fourier transforming Eqs (8) and (9), one then obtains

$$Q(\omega) = \Lambda(\omega)Q(\omega) + N(\omega), \quad (10)$$

$$Q(\omega) = T(\omega)N(\omega), \quad (11)$$

where ω is the angular frequency. This equation also describes evoked response potentials, whereby a known stimulus is input and the response $Q(\omega)$ is measured. Since the system is linear, the evoked response adds linearly to any background activity driven by other inputs; we return to this in more detail in Sec. 2.2.3.

To avoid any notational ambiguity, we define the Fourier transform and its inverse via

$$g(\omega) = \int_{-\infty}^{\infty} g(t)e^{i\omega t} dt, \quad (12)$$

$$g(t) = \int_{-\infty}^{\infty} g(\omega)e^{-i\omega t} \frac{d\omega}{2\pi}. \quad (13)$$

Equations (10) and (11) imply

$$T(\omega) = [I - \Lambda(\omega)]^{-1}, \quad (14)$$

where I is the identity matrix and the superscript -1 represents matrix inversion.

We can expand Eq. (14) in powers of Λ to give

$$T(\omega) = I + \Lambda(\omega) + \Lambda^2(\omega) + \Lambda^3(\omega) + \dots, \quad (15)$$

and thus

$$Q(\omega) = [I + \Lambda(\omega) + \Lambda^2(\omega) + \Lambda^3(\omega) + \dots]N, \quad (16)$$

both of which converge provided all the eigenvalues λ_j of Λ satisfy $|\lambda_j| < 1$.

Equation (16) expresses Q as the sum of different interactions, with each term represented by Feynman diagrams shown in Fig. 1. Each term describes activity evoked by external inputs, with the IN term expressing direct external input, the ΛN term expressing external input that

has entered, then been propagated directly to another point, the $\Lambda^2 N$ term expressing external input that has entered, then been propagated to another point via one intermediate point, and so on. This explicitly describes the behavior of the system in which external stimulation of any point produces activity that then propagates to other points throughout the system via both direct and indirect paths.

If linear convolutional measurement processes further intervene between Q and some measured signal X , these can be represented by a further transfer function Z such that

$$X(\omega) = Z(\omega)T(\omega)N(\omega), \quad (17)$$

$$= H(\omega)N(\omega), \quad (18)$$

in a similar notation to Dhamala et al., 2008.

Often one is interested in measurement methods that detect signals that are chiefly due to activity of the pyramidal neurons in the cortex, such as electroencephalography, magnetoencephalography, and functional magnetic resonance imaging (Kahn et al., 2011; Logothetis et al., 2001; Silva, 2013). In this case, one can assign the first population label to these neurons and focus on the leading $M \times M$ transfer matrix, but it is essential to note that this depends on the whole $MP \times MP$ direct connectivity matrix Λ . In the cortex, only the pyramidal cells provide fast long-range communication across the cortex, whereas the other cortical and subcortical (e.g., interneuron and thalamic neuron) populations are involved in short-range dynamics, often at spatial scales below those of the experimental discretization and we therefore do not observe these populations and local connectivities directly (Robinson, 2019). The reduced transfer function thus provides a representation in terms of a single effective population, with connectivity determined by the pyramidal connections, and local dynamics by all populations, as illustrated in Fig. 2. To simplify notation, from this point on we assume only a single population of interest, and thus discontinue using population subscripts.

2.2. Importance of the transfer function

Measurement of the full experimentally discretized transfer function involves evaluating $M \times M$ elements at each frequency (or time difference), whose measurement imposes a computational burden of order M^2 . Before discussing how T can be evaluated from less than $O(M^2)$ measurements per frequency, we first justify the effort by briefly summarizing the importance of T to quantifying and interrelating a wide variety of experimental measures of brain activity and structure.

The transfer function of a system contains complete information about its linear properties, responses, and dynamics. Thus all measures and analyses of the system's linear properties can be obtained and performed once the transfer function is known, in combination with knowledge of, or assumptions about, the input. Below we detail some of these important relationships between the transfer function and measures and analysis of brain dynamics. In doing so we highlight the central importance and usefulness of the transfer function, including its ability to interrelate and synthesize a variety of results while also providing direction for further analysis.

2.2.1. Spectra and coherence

The first quantity that can be calculated from Q is the cross spectrum

$$C(\mathbf{r}, \mathbf{r}', \omega) = \langle Q(\mathbf{r}, \omega)Q^*(\mathbf{r}', \omega) \rangle, \quad (19)$$

which is equivalent to the Fourier transformed correlation matrix (described below), and which gives the power spectrum if $\mathbf{r} = \mathbf{r}'$. The angle brackets in Eq. 19 represent an average over experimental trials.

In matrix notation, Eq. 19 can be written

$$C(\omega) = \langle Q(\omega)Q^\dagger(\omega) \rangle, \quad (20)$$

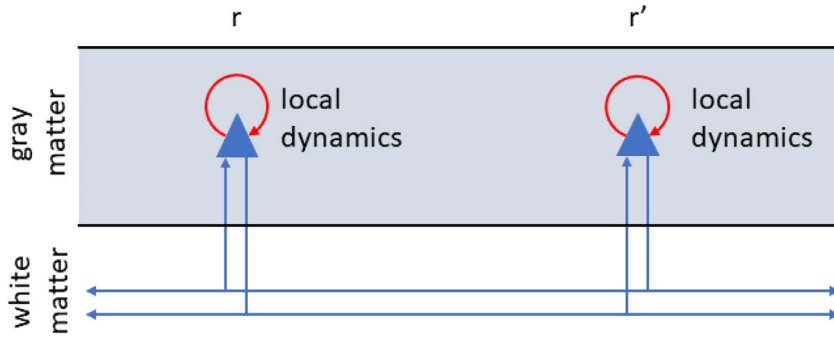


Fig. 2. Excitatory pyramidal neurons (blue triangles) found throughout the cortical sheet (shaded) are the major source of signals for measurement modalities such as EEG and fMRI. These neurons couple distant points r and r' with long range white-matter projections. The pyramidal neurons are also coupled to other local populations of nearby neurons that are not directly measured, but whose activity (red) influences pyramidal neuron activity and is therefore encoded in the measured signal from the excitatory pyramidal neurons. Thus, the resulting transfer function estimated from these signals is for the transfer between points in the pyramidal populations and their coupled local population dynamics, not the transfer between points in the pyramidal population alone.

$$= T(\omega)\langle N(\omega)N^\dagger(\omega)\rangle T^\dagger(\omega), \quad (21)$$

where the dagger denotes the Hermitian conjugate.

In the commonly considered case of “resting-state” activity in which no task is imposed by an experimenter and the subject is in relaxed surroundings, background stimuli span a broad range of spatial and temporal scales after passing through the peripheral nervous system, which also tends to whiten them to make best use of available bandwidth. Consequently, numerous applications to experimental data have shown that background perturbations can be approximated by spatially uncorrelated white noise (Abeyseriya et al., 2015; Deco et al., 2008; Robinson et al., 1997, 2002; van Albada et al., 2010). In the case of uncorrelated white noise inputs one has $\langle N(\omega)N^\dagger(\omega)\rangle = I$, so

$$C(\omega) = T(\omega)T^\dagger(\omega). \quad (22)$$

The coherence function in coordinate space is given by

$$\gamma^2(\mathbf{r}, \mathbf{r}', \omega) = \frac{|C(\mathbf{r}, \mathbf{r}', \omega)|^2}{C(\mathbf{r}', \mathbf{r}', \omega)C(\mathbf{r}, \mathbf{r}, \omega)}. \quad (23)$$

In matrix notation, the coherence between points \mathbf{r}_i and \mathbf{r}_j is

$$\gamma_{ij}^2(\omega) = \frac{|C_{ij}(\omega)|^2}{C_{ii}(\omega)C_{jj}(\omega)}. \quad (24)$$

The transfer function describes causal propagation of influences of one element of the system on another. This can be used to understand causality in the system in conjunction with knowledge of the input drive. An often used measure is Granger Causality. Formally, spectral Granger Causality is an inferred measure of directional influence from one time series to another and is based on linear predictions of time series (Dhamala et al., 2008). The Granger influence of the point indexed by j on the point indexed by i is expressed in matrix notation as

$$I_{ij}(\omega) = \ln \left[\frac{C_{ii}(\omega)}{C_{ii}(\omega) - \left(\sigma_{jj} - \frac{\sigma_{ij}^2}{\sigma_{ii}} \right) |T_{ij}(\omega)|^2} \right], \quad (25)$$

where σ is the matrix of input covariances. Inputs are *not* assumed to be uncorrelated white noise in computing Granger Causality.

2.2.2. Correlations and covariance

We define the correlation of activity between points \mathbf{r}_i and \mathbf{r}_j as

$$C(\mathbf{r}_i, \mathbf{r}_j, \tau) = \left\langle \int Q(\mathbf{r}_i, t + \tau)Q(\mathbf{r}_j, t)dt \right\rangle, \quad (26)$$

where τ is the time difference between the correlated measurements and the angle brackets denote an average over realizations. The matrix form of (26) is written

$$C(\tau) = \left\langle \int Q(t + \tau)Q^T(t)dt \right\rangle. \quad (27)$$

The Wiener-Khinchine Theorem states that the correlation $C(\tau)$, and cross spectrum $C(\omega)$ are Fourier transforms of one another; i.e.,

$$C(\tau) = \frac{1}{2\pi} \int_{-\infty}^{+\infty} e^{-i\omega\tau} C(\omega)d\omega, \quad (28)$$

and

$$C(\omega) = \int_{-\infty}^{+\infty} e^{i\omega\tau} C(\tau)d\tau. \quad (29)$$

It should be noted that the definitions of correlation and covariance vary in the literature so care must be taken in comparing theory and results from different sources. Other common definitions of correlation and covariance involve first subtracting mean values from the time series, and/or normalizing time series by dividing by their standard deviations. These can all be evaluated by similar means.

2.2.3. Evoked responses

Studies of evoked changes in brain activity probe the response of the brain to a given stimulus by tracing the propagation of evoked activity away from the source of the stimulus. Identifying these responses can then be used to infer aspects of the processing that occurs during this propagation for each particular stimulus (Fox et al., 2006; Kerr et al., 2008, 2011; Luck and Kappenman, 2012).

If the character of the stimulus is well known or approximated and the transfer function is known, then the system response is given by Eqs (3), (7), (9), or (11), depending on the notation used. In experiments on evoked response potentials (ERPs), brief stimuli are often presented. Such a stimulus can be approximated as a delta function in time. In matrix notation, this stimulus can be written as $N(t) = \delta(t - t_0)N_0$, where t_0 is the time that the stimulus is applied, and N_0 is a vector describing the strength and spatial structure of the stimulus (Mukta et al., 2019; 2020). The response to this stimulus is

$$Q_{ERP}(t) = T(t - t_0)N_0, \quad (30)$$

or, in Fourier form,

$$Q_{ERP}(\omega) = T(\omega)e^{i\omega t_0} N_0. \quad (31)$$

Note that if N_0 is a delta function in space, (30) demonstrates that the ERP measures the transfer function.

In steady state evoked potential (SSEP) experiments, periodic stimuli are presented (Norcia et al., 2015). The simplest periodic stimulus is

$$N(t) = \cos[\omega_0(t - t_0)]N_0, \quad (32)$$

which ignores any initial transient period, and where ω_0 is the stimulus frequency and N_0 describes its strength and spatial structure. The temporal Fourier transform of this stimulus is

$$N(\omega) = \pi e^{i\omega t_0} [\delta(\omega - \omega_0) + \delta(\omega + \omega_0)]N_0, \quad (33)$$

and the response is given by Eq. (11)

$$Q_{SSEP}(\omega) = \pi e^{i\omega t_0} [\delta(\omega - \omega_0) + \delta(\omega + \omega_0)]T(\omega)N_0, \quad (34)$$

which can be inverse Fourier transformed to give

$$Q_{SSEP}(t) = \cos(\omega_0[t - t_0])T(\omega_0)N_0. \quad (35)$$

Because Q is proportional to EEG measurements, this is the sinusoidally varying response in time seen in experiments (Nordia et al., 2015). The response to more complex periodic stimuli, $N(t)$, can be obtained by Fourier transforming to give $N(\omega)$, then inverse Fourier transforming the RHS of Eq. (11), or alternatively by directly solving Eq. (9).

2.2.4. Structure-Function relationships and eigenmodes

All activity can be expressed in terms of the physical eigenmodes of a system, providing a systematic basis for wider-ranging physical analyses, statistical quantities such as “resting state networks” (RSNs), and conceptual and practical advances more generally (Gabay et al., 2018; Gabay and Robinson, 2017; Robinson et al., 2016). Notably, eigenmodes differ in a fundamental way from the statistical components inferred via methods like ICA and PCA. Eigenmodes are entities that derive from the dynamics of the brain as the physical system that generates observed activity, and their nature is directly related to brain anatomy and physiology; in contrast, ICA and PCA components are entities that are obtained from time series without regard to the nature of the system that generates them or the physical quantities they represent. Statistical measures can be useful, but this fundamental difference must be borne in mind.

The eigenfunctions of a system describe specific patterns of activity whose spatial structure is fixed, but whose amplitude can change over time. Thus, the eigenfunctions (often called eigenmodes, natural modes, or eigenvectors) of a system are useful quantities for describing and analyzing its activity. The structure of a system’s eigenfunctions are determined by its dynamics and spatial properties.

If the structure of a system is constant in time its spatial and temporal dynamics are separable, so its eigenfunctions, labeled n , each has the form of a constant spatial eigenfunction $v_n(\mathbf{r})$ multiplied by a temporal factor, which is a complex exponential (or equivalently a trigonometric function) at each angular frequency ω , $\exp(-i\omega t)$. In matrix notation v_n can be viewed as a column vector with one entry for each point into which the system has been approximately discretized.

If T is diagonalizable, we can perform a spectral decomposition (i.e., an eigenfunction decomposition) of T to express T in terms of its eigenvalues and eigenvectors, with

$$T(\omega) = V\Theta(\omega)V^{-1}, \quad (36)$$

where $\Theta(\omega)$ is a diagonal matrix containing the eigenvalues $\theta_n(\omega)$ of $T(\omega)$, and V is a matrix whose columns are the spatial eigenvectors v_n of $T(\omega)$. Note that the reality condition requires that $T^*(\omega) = T(-\omega)$.

Similarly we can decompose the propagator Λ as

$$\Lambda(\omega) = UL(\omega)U^{-1}, \quad (37)$$

where U and L are the matrices of eigenvectors and eigenvalues of Λ , respectively, with L being diagonal. Equations Eq. (14) and (15) each demonstrates that the eigenvectors of T and Λ are the same. Using Eq. (14), the eigenvalues λ_n of Λ are then related to the eigenvalues θ_n of T by

$$\theta_n(\omega) = [1 - \lambda_n(\omega)]^{-1}. \quad (38)$$

We can also spectrally decompose C to give

$$C(\omega) = WK(\omega)W^{-1}, \quad (39)$$

where W and K are the matrices of eigenvectors and eigenvalues of C , respectively, with K being diagonal. From Eq. (20), we see that C is Hermitian, so its eigenvalues are real and its eigenvectors form a complete orthonormal set. If T is also Hermitian, the eigenvectors of C are the same as those of T and Λ (i.e., $U = V = W$) and the eigenvalues of C , κ_n , are related to those of T and Λ by

$$\kappa_n(\omega) = |\theta_n(\omega)|^2 = \left| \frac{1}{1 - \lambda_n(\omega)} \right|^2. \quad (40)$$

3. Results

The above sections have established the importance of the transfer function in brain analysis at the mesoscale and above. The aim of this

section is to describe methods for obtaining the transfer function from experimental data.

3.1. Determination of the transfer function

Below we describe how a transfer function can be obtained from evoked responses, modal projection of eigenmodes, and spectral factorization. The advantages and disadvantages of these methods are described.

3.1.1. Direct measurement via ERPs

One way to measure a brain transfer function is to use evoked response potentials (ERPs). The response to a known delta-function stimulus is by definition the transfer function $T(r, r_0, t)$ to the measurement point r , from the stimulated point r_0 (Mukta et al., 2019; 2020). However, to determine the full transfer function between all pairs of points, these measurements must be made for stimuli at each point in turn, making this a laborious process that requires $M \times M$ measurements for M points. A further difficulty arises in ensuring the strength of the stimulus is equal at each point, or known precisely, so that T is normalized consistently.

3.1.2. Modal projection

High spatial resolution measurements of brain activity can be obtained using BOLD (blood-oxygenation level dependent) fMRI; however, fMRI has very low temporal resolution for neural events. In contrast, EEG has low spatial resolution, but high temporal resolution. These two types of measurements can be combined using modal projection to estimate T . This method was first presented in Robinson (2019), and we provide more detail here.

In the case where T is Hermitian and its eigenfunctions form a complete orthonormal set, activity can be expanded as Robinson (2019)

$$Q(\mathbf{r}, t) = \sum_j u_j(\mathbf{r})c_j(t), \quad (41)$$

$$c_j(t) = \int Q(\mathbf{r}, t)u_j(\mathbf{r})d\mathbf{r}, \quad (42)$$

in coordinate notation, where the integral is over the whole domain and the $u_j(\mathbf{r})$ are assumed to be real without loss of generality.

The quantity $T(\mathbf{r}, \mathbf{r}_0, t)$ is, by definition, the response at \mathbf{r} and t to a delta-function input at \mathbf{r}_0 and $t = 0$. In this case, $c_j(0) = u_j(\mathbf{r}_0)$, so

$$T(\mathbf{r}, \mathbf{r}_0, t) = \sum_j u_j(\mathbf{r})u_j(\mathbf{r}_0)\theta_j(t), \quad (43)$$

which is equivalent to the temporal Fourier transform of (36) in the present case where $U = V$. Hence Robinson (2019),

$$\theta_j(t) = \frac{1}{u_j(\mathbf{r}_0)} \int T(\mathbf{r}, \mathbf{r}_0, t)u_j(\mathbf{r})d\mathbf{r}. \quad (44)$$

Calculation of the integral in Eq. (44) is problematic, at least for EEG and ERP, because it is difficult to measure activity inferior to the cortex and in sulci. However, analogously to the fact that L Fourier modes can be sampled with L measurement points, not necessarily equally spaced, it has been pointed out that the same can be done with eigenmodes (Robinson, 2013). Specifically, we first restrict ourselves to the lowest L modes, choose a stimulus point \mathbf{r}_0 and measurement points r_k with $k = 1, \dots, L$.

The first step is to use a technique, such as fMRI, that has fine spatial resolution, to obtain the set of orthonormal eigenmodes $u_j(\mathbf{r})$ via standard eigenfunction analysis of the covariance matrix, which is the equal-time correlation matrix with $\tau = 0$ in Eq. (27). The next step is to apply a delta-function stimulus at \mathbf{r}_0 and to measure the evoked responses $a_k(t)$ at the \mathbf{r}_k using a fast method such as EEG. From the definition of the transfer function and from the eigenfunction decomposition in Eq. (43) we define the quantities $a_k(t)$ as

$$a_k(t) = T(\mathbf{r}_k, \mathbf{r}_0, t), \quad (45)$$

$$\approx \sum_{k=1}^L u_j(\mathbf{r}_k) u_j(\mathbf{r}_0) \theta_j(t), \quad (46)$$

$$= \sum_{k=1}^L b_{kj} \theta_j(t), \quad (47)$$

where the eigenfunctions are obtained via the diagonalization in Eq. (39), $b_{kj} = u_j(\mathbf{r}_k) u_j(\mathbf{r}_0)$, and we have truncated the sum at L modes.

Equation (47) and its solution can be written in matrix form as

$$A(t) = B\Theta(t), \quad (48)$$

$$\Theta(t) = B^{-1}A(t), \quad (49)$$

where $A(t)$ and $\Theta(t)$ are L -element column vectors of $a_k(t)$ and $\theta_j(t)$ and the elements of the $L \times L$ matrix B are the b_{kj} . By this means we can combine eigenfunctions obtained by slow measurements throughout the brain (e.g., fMRI) with L fast measurements (e.g., via EEG) at accessible parts of the brain to approximate the transfer function via Eqs (36) and (49). The key restriction in addition to the assumed symmetry of the system is that B should not have too large a condition number, which would occur if some of the stimulus or measurement points were located very close to eigenfunction nodes, for example, causing a whole row or column of B to have near-zero entries and thus making it near-singular.

3.1.3. Spectral factorization of cross spectra

An alternative route to obtaining the transfer function from experimental measurements is to use correlations of measured activity, which are relatively simple to obtain experimentally. However, if we have $C(\omega)$, solving Eq. (22) for $T(\omega)$ implies a process akin to taking a matrix square root of $C(\omega)$ to find $T(\omega)$. For an $n \times n$ matrix with n distinct eigenvalues there are 2^n square roots (Horn and Johnson, 2013), only one of which corresponds to T .

To find the solution for T that corresponds to the delta-function response of the underlying physical system, spectral factorization algorithms can be applied to $C(\omega)$. Here we focus on the Wilson algorithm (T. Wilson, 1972), which uses an iterative root finding approach to construct a minimum-phase solution which makes the physically realistic assumption that the underlying physical system is stable, and causal. Physically, a minimum-phase solution minimizes the system's group delay (Smith et al., 2007), meaning that the response to a delta function is in phase for all frequencies at the stimulus point and is thus initially as compact as possible in time.

The Wilson algorithm has previously been used as a step in computing Granger causality (Dhamala et al., 2008a,b), but its importance as a means of obtaining the system transfer function has not been appreciated and used to exploit the myriad relationships the transfer function has to other measures, models, and applications as described in Section 2. Other spectral factorization algorithms do exist, including that of Janashia et al. (Ephremidze et al., 2008, 2018).

A technical point on this implementation of the Wilson algorithm is that it involves performing a Cholesky decomposition on the input C matrix (Horn and Johnson, 2013). Cholesky decomposition of a matrix requires the matrix to be positive definite (symmetric matrices with all real, positive eigenvalues). As described in Section 2.2.4, $C(\omega)$ should be positive definite; however, numerical round-off errors in $C(\omega)$ can introduce small negative eigenvalues, which causes the Cholesky factorization to fail. In these cases, our implementation of the algorithm reverts to an alternate approach that uses matrix inverses. The method of using Cholesky decomposition is preferred due to superior numerical precision compared to a numerical matrix inverse. Our code implementing the Wilson Algorithm can be found at <https://github.com/BrainDynamicsUSYD/SpecFac>.

The scaling of the Wilson algorithm runtime with the number of frequencies and spatial samples is an important practical consideration in obtaining T from time series measurements. The Wilson algorithm is noted for its numerical efficiency (Dhamala et al., 2008; Ephremidze et al., 2018). The dominant runtime cost of the Wilson algorithm lies in steps involving Cholesky Factorization and solving linear systems (or alternatively matrix inversion, depending on the implementation), as well as matrix multiplication. Since a fixed number of these operations are required per iteration of the algorithm, the runtime per iteration should scale as M^μ for an M -node system. Simple algorithms for performing these operations have $\mu = 3$ for inversion via Gaussian elimination or LU factorization, for example; however, more sophisticated algorithms have $\mu \approx 2.81$ for the Strassen algorithm (Huang et al., 2016; Strassen, 1969) or as little as $\mu \approx 2.37$ for optimized Coppersmith-Winograd algorithms (Coppersmith and Winograd, 1990), although the latter have yet to be practically implemented. For n_t frequency samples, the theoretical scaling of the runtime per step is

$$t_{step} \sim n_t M^\mu. \quad (50)$$

Note that if the number of iterations required for convergence also depends on M or n_t , a further factor would need to be included in this result.

3.2. Sampling criteria

Before proceeding to test the spectral factorization algorithm, we summarize the criteria that must be satisfied if T is to be accurately inferred for a given physical system.

Suppose we have a system whose transfer function is desired to be calculated with spatial and temporal resolutions of δx and δt , respectively. Suppose, furthermore that we wish to obtain the estimate T_{est} of T over a time t_{max} and spatial region of width x_{max} . The first constraint is that

$$vt_{max} \leq x_{max}, \quad (51)$$

if v is the characteristic velocity of the response; otherwise the response will exit the system. An exception is if the system is closed and boundaries are periodic, for example, in which case larger t_{max} may be relevant to follow the long-term decay of the response.

We seek criteria for the numbers of required sampling points n_x required in x (assuming a 1D system for the moment, with direct generalization to multiple dimensions) and n_t in t , corresponding sampling resolutions Δx and Δt , and maximum frequency f_{max} and resolution Δf when working in the temporal Fourier domain, with the usual relationship between temporal and angular frequencies, $\omega = 2\pi f$. These are:

(i) Δx and Δt must be less than or equal to the above δx and δt , respectively.

(ii) The condition

$$v\Delta t \leq \Delta x, \quad (52)$$

must also be satisfied to enable fine spatial features to be resolved.

(iii) Hence, the numbers of points in each spatial dimension and in time must be at least

$$n_x = x_{max}/\Delta x \geq x_{max}/\delta x, \quad (53)$$

$$n_t = t_{max}/\Delta t \geq t_{max}/\delta t, \quad (54)$$

respectively.

(iv) A time resolution Δt implies a temporal sampling rate $1/\Delta t$. Hence, via Nyquist's theorem, we sample a maximum frequency in the Fourier domain of

$$f_{max} = 1/(2\Delta t), \quad (55)$$

with a frequency resolution of

$$\Delta f = 1/t_{max}. \quad (56)$$

For convenience, we also note that Eqs (52) and (55) imply that one must choose

$$f_{\max} \geq \frac{v}{2\Delta x}. \quad (57)$$

(v) As is demonstrated in the test cases below, the Wilson algorithm tends to produce its largest errors for $t \approx t_{\max}/2$. Thus, if an estimate of T is desired up to a maximum time delay t_d , one may wish to set

$$t_{\max} > 2t_d. \quad (58)$$

We discuss below how errors, including near $t_{\max}/2$ approach zero as t_{\max} increases and Δt decreases simultaneously.

Equations (51) – (58) summarize the sampling requirements to treat a system with the size, duration, and resolution mentioned above. However, if sampling is limited to lower rates and/or coarser spatial resolution, these equations can be rearranged to calculate the achievable resolutions in space, time, and frequency.

Perfectly uniform spatial sampling is desirable, but not possible in practice; many cortical parcellations contain non uniformly sized and shaped regions of interest. Thus, these criteria represent worst-case requirements that may be able to be relaxed depending on specifics of the sampling. Note that these criteria do not eliminate pitfalls of spectral analysis, like aliasing, nor guarantee good estimation of T for any particular experimental modality because artefacts and noise are often present in data. These issues must be address separately on a case by case basis.

3.3. Tests of factorization of brain activity cross spectra to obtain transfer functions

This section demonstrates the estimation of system transfer functions from cross spectra using the Wilson Spectral Factorization algorithm (Dhamala et al., 2008; T. Wilson, 1972). We demonstrate this using a series of increasingly difficult test cases that introduce realistic system features such as asymmetry [i.e., $\Lambda(\mathbf{r}, t, \mathbf{r}', t') \neq \Lambda(\mathbf{r}', t, \mathbf{r}, t')$], two dimensionality of the system, time delays, and complex network connectivity. These increasingly brain-like test cases imply that the algorithm will produce accurate results when applied to data of the complexity obtained in current experiments.

The procedure for testing the Wilson spectral factorization algorithm is illustrated in Fig. 3. First, Λ is chosen for each test case, then the transfer function $T(\omega)$ is computed using Eq. (14), followed by the cross spectrum $C(\omega)$ via Eq. (22) which assumes the system is driven by white noise that is spatially uniform in strength; however, the algorithm produces an estimate of the input spectral density matrix $N(\omega)N^\dagger(\omega)$, so the assumption of uniform white noise is not required in general. Note that no changes to C are made to remove global signals, or modify diagonal elements, as often occurs in analyses of fMRI data, for example (Liu et al., 2017). Then the cross spectrum is input to the Wilson algorithm, whose transfer function estimate T_{est} is compared to the actual transfer function T . The difference between T and T_{est} is quantified as

$$\epsilon = \frac{\sqrt{\sum |T - T_{\text{est}}|^2}}{\sqrt{\sum |T|^2}}. \quad (59)$$

Parseval's theorem implies that ϵ has the same value when computed using T in either the temporal or frequency domain. The sums are over all frequencies or timepoints, and all elements in the transfer function matrix. If only the initial timepoints of $T_{\text{est}}(t)$ are used to avoid the largest error around $t_{\max}/2$, then ϵ will be smaller over the reduced temporal range, but Parseval's theorem no longer holds to allow the same value to be obtained by computing ϵ in the frequency domain.

We examine the accuracy of estimation as a function of sampling parameters and, to test the robustness of the algorithm to measurement noise, we quantify the effects of adding random noise to Q , which is linearly related to measurements, before constructing $C(\omega)$ as input to the algorithm.

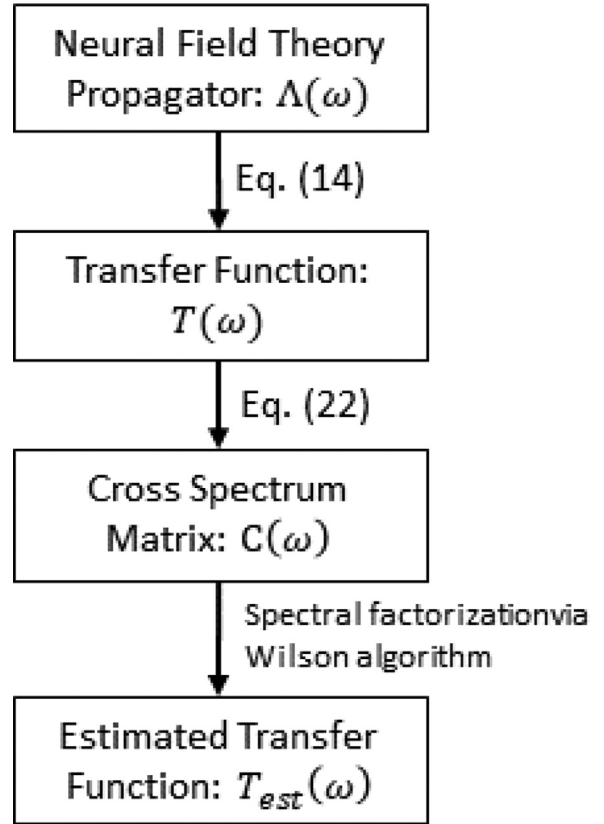


Fig. 3. The procedure for testing the Wilson spectral factorization algorithm. A known propagator is used to produce a known transfer function, followed by the cross spectrum for input into the Wilson algorithm. The estimated transfer function output from the algorithm is compared to the known transfer function.

Table 1

Parameter values used in the test cases (Robinson et al., 1997). The first to fourth columns list the quantity, its symbol, nominal value, and unit, respectively.

Quantity	Parameter	Value	Unit
Decay rate	γ	107	s^{-1}
Axonal velocity	v	9	$m s^{-1}$
Synaptic decay rate	α	100	s^{-1}
Synaptic rise rate	β	350	s^{-1}
Axonal range	r_c	84	mm

3.3.1. Asymmetric 1D transfer function estimation

We first test the ability of the Wilson spectral factorization algorithm to estimate the transfer function for asymmetric systems (i.e., where $T_{ij} \neq T_{ji}$) with fine-scale dynamics and the resulting dependencies on sampling parameters and noise.

Transfer Function Estimation We use a 1D system with simple dynamics described by an impulse response that consists of two dissipative δ functions propagating in opposite directions with velocity v and damping rate γ after a δ function input at $(X, \tau) = (0, 0)$:

$$\Lambda(X, \tau) = Ge^{-\gamma\tau}[(1 + \eta)\delta(X - v\tau) + (1 - \eta)\delta(X + v\tau)], \quad (60)$$

in coordinate space, where $-1 \leq \eta \leq 1$ governs the degree of asymmetry, with symmetry for $\eta = 0$ and full asymmetry for $\eta = \pm 1$ (Robinson, 2012). Here we use $\eta = -0.5$ and G is a gain chosen so that the largest eigenvalue of Λ is $\lambda_1 = 0.85$, ensuring the system is stable but near criticality, as in the brain (Robinson et al., 2002). Parameter values are given in Table 1.

Because Λ consists of delta functions it has no lower bound on δt and δx . However, we choose to use periodic boundary conditions and

set $x_{\max} = 150$ mm and $\Delta x = 3$ mm, thereby forgoing any finer resolution; hence, $n_x = 50$. We then impose the condition (57) to set $\Delta t = 0.33$ ms. With a damping rate of $\gamma = 107 \text{ s}^{-1}$, *direct* propagation of activity has an e-folding timescale of 9.3 ms. However, overall activity in the system decays on a longer timescale due to internal regeneration during indirect propagation that contributes to T , as in Eq. (15). This timescale becomes very long when T is close to critical because there is stronger internal regeneration of activity (Robinson, 2012). This is described mathematically in Eq. (15) whereby higher powers of Λ decay more slowly near criticality. Numerical calculations show that this extends the decay time to 44 ms. From these considerations we choose $t_{\max} = 0.26$ s which is 6 times the decay time, giving $n_t = 789$.

The above values imply that the Wilson algorithm needs as input the correlation functions at n_t frequencies from $-f_{\max} + \Delta f$ to f_{\max} with $f_{\max} = 1/(2\Delta t) = 1500$ Hz and $\Delta f = 1/t_{\max} \approx 3.8$ Hz.

Given $\Lambda(\omega)$, Eq. (14) is used to construct the transfer function $T(\omega)$ which allows the cross spectrum $C(\omega)$ to be computed using Eq. (22), assuming white noise input. The resulting $C(\omega)$ is input to the Wilson spectral factorization algorithm to compare its estimated transfer function $T_{\text{est}}(\omega)$ with the actual one.

As noted earlier, T and Λ correspond to responses to temporal delta function inputs, with each able to be calculated from the other via Eq. (14). Thus, to visualize $T(X, \tau)$ and $\Lambda(X, \tau)$, we plot the response to a delta function. Figs. 4(a) and (b) show T and Λ , respectively. The propagation of the delta functions away from the stimulus location can be seen, as can the asymmetry between leftward and rightward propagation. Because the system is translationally invariant, responses to inputs at different points have the same form, but shifted in space. In Figs. 4(c) and (d) examples are shown of $T(\tau)$ and $\Lambda(\tau)$ at a point separated from the stimulus by 0.051 m. In Figs 4(c) and (d) there are two δ pulses corresponding to propagation arriving from the leftward and rightward propagating activity, with the later pulse having passed through the periodic boundary. The T response in Fig. 4(c) differs from Λ in Fig. 4(d) by containing additional responses at later timepoints than are shown, resulting from internal regeneration of activity and activity looping through the system's periodic boundaries. Figs. 4(e) and (f) show the differences between T and T_{est} , and between Λ and Λ_{est} , respectively. The largest errors are at $t_{\max}/2$, shown by the two central positive and negative peaks. This error is predominantly due to the use of truncated Fourier series in the numerical implementation of the Wilson algorithm, rather than infinite Fourier series in the mathematical derivation of the Wilson algorithm. Only features that are robust with respect to t_{\max} should be interpreted as features of the underlying system. The errors are highly oscillatory, but the oscillations are not resolved in the figure. This error can be reduced by increasing t_{\max} (equivalent to reducing Δf) and approaches zero (as we see below).

Dependence of Accuracy on Sampling Parameters To obtain greater insight into the performance of the algorithm as a function of its sampling parameters and to check the criteria for time series sampling described in Section 3.2, we now test how the error ϵ at fixed x_{\max} and Δx depends on Δt and t_{\max} , with f_{\max} and Δf given by Eqs (55) and (56).

Fig. 5 (a) shows how ϵ depends on Δt with t_{\max} fixed; the value used in Fig. 4, and given by equality in Eq. (52) is indicated by the red arrow. As Δt increases, the fast dynamics of the system are increasingly missed so ϵ increases. Fig. 5(b) shows ϵ vs. t_{\max} for fixed Δt , with the red arrow indicating the point that corresponds to the value of t_{\max} used in Fig. 4. We see that as t_{\max} is increased, ϵ decreases, chiefly due to the reduction of the errors at $t \approx t_{\max}/2$. This indicates that t_{\max} should be chosen to be larger than the slowest responses of the system that are of interest to minimize errors, as described by Eq. (58). However, this is not necessary if only short-time responses are of interest in a particular situation — e.g., the period before signals reach the system boundaries.

The dips in Fig. 5(a) and (b) near the red arrows are artefacts of the delta function propagator and spatially discretized system where Δt and t_{\max} transition from integer to non integer multiples of the propagation time delay between points and are not relevant to real brains.

Dependence of Accuracy on Noise We next test the accuracy of the algorithm in the presence of measurement noise. To do so, we introduce additive white noise to $Q(\omega)$:

$$Q'(\omega) = Q(\omega) + cY(\omega), \quad (61)$$

where $Y(\omega)$ represents noise and c is a constant that scales the magnitude of the noise.

From this and Eq. (20), the cross spectrum of the noisy measurements Q' is

$$C'(\omega) = T\langle NN^\dagger \rangle T^\dagger + c\langle YN^\dagger \rangle T^\dagger + cT\langle NY^\dagger \rangle + c^2\langle YY^\dagger \rangle. \quad (62)$$

If both N and Y are uncorrelated white noise signals, Eq. (62) reduces to

$$C'(\omega) = TT^\dagger + c^2I. \quad (63)$$

We therefore use Eq. (63) to test the ability of the algorithm to estimate $T(\omega)$ when additive white noise is present. Fig. 5(c) shows how ϵ scales with c for the same 1D system as in Fig. 4. When $c = 0$ there is no noise and $\epsilon = 0.022$ as above. As c increases, ϵ increases approximately linearly, reaching $\epsilon \approx 0.09$ when $c = 1$ and the measurement noise equals the strength to the system input noise; after this the error increases more slowly until measurement noise dominates, $C' \approx c^2I$, and $T_{\text{est}} \approx cI$ so information about the actual system is lost.

3.3.2. Transfer function estimation for a 2D neural field propagator

The cortex is an approximately 2D system with area of around 2000 cm^2 , but a thickness of only a few mm (Kandel et al., 2012). We therefore need to test the ability of the algorithm to estimate transfer functions for 2D systems with realistic brain dynamics.

Transfer Function Estimation

The wave equation component of a commonly used neural field propagator on a 2D plane is given by Robinson (2012); Robinson et al. (1997)

$$\Gamma(\mathbf{r}, \omega) = \frac{1}{2\pi r_e^2} K_0 \left[\frac{R}{r_e} \left(1 - \frac{i\omega}{\gamma} \right) \right], \quad (64)$$

where $R = |\mathbf{r}|$.

When a pulse arrives at a point, further dynamics for the temporal spread and conduction delay of pulses within local dendritic trees and soma responses have the form Robinson et al. (1997)

$$\mathcal{L}(\omega) = (1 - i\omega/\alpha)^{-1}(1 - i\omega/\beta)^{-1}, \quad (65)$$

where $\alpha = 100 \text{ s}^{-1}$ and $\beta = 350 \text{ s}^{-1}$ are time constants that govern the rise and fall of these dynamics.

The full propagator for the system combines these synaptic dynamics with the temporal Fourier transform of the 2D delta function propagator in Eq. (64) to give

$$\Lambda(\mathbf{r}, \omega) = G\mathcal{L}(\omega)\Gamma(\mathbf{r}, \omega), \quad (66)$$

where as in the 1D case, G is a gain chosen so that the largest eigenvalue of Λ is 0.85 and the system is close to critical, as in real brains (Robinson et al., 2002).

In our numerical work we use a 470×470 mm system with periodic boundary conditions, giving it an area consistent with that of the brain and obviating the constraint (51) on t_{\max} . We discretize into a 17×17 grid of $M = 289$ points, giving $n_x = 17$ and $\Delta x = 27.6$ mm so physical features below this level are not resolvable. For this discretization, Eq. (52) implies $\Delta t \lesssim 3.1$ ms or $f_{\max} = 162$ Hz, which we use here.

In the present system the combined synaptic, dendritic, and soma dynamics act as a low pass filter, embodied in the factor $\mathcal{L}(\omega)$ in Eq. (65). This strongly attenuates angular frequencies below a few times α^{-1} , corresponding to a few times 10 Hz for the parameters in Table I. Based on this, Δt could be increased to say, $\Delta t = 10$ ms or $f_{\max} = 50$ Hz, which suffices to capture most of the system response if resolving T with finer

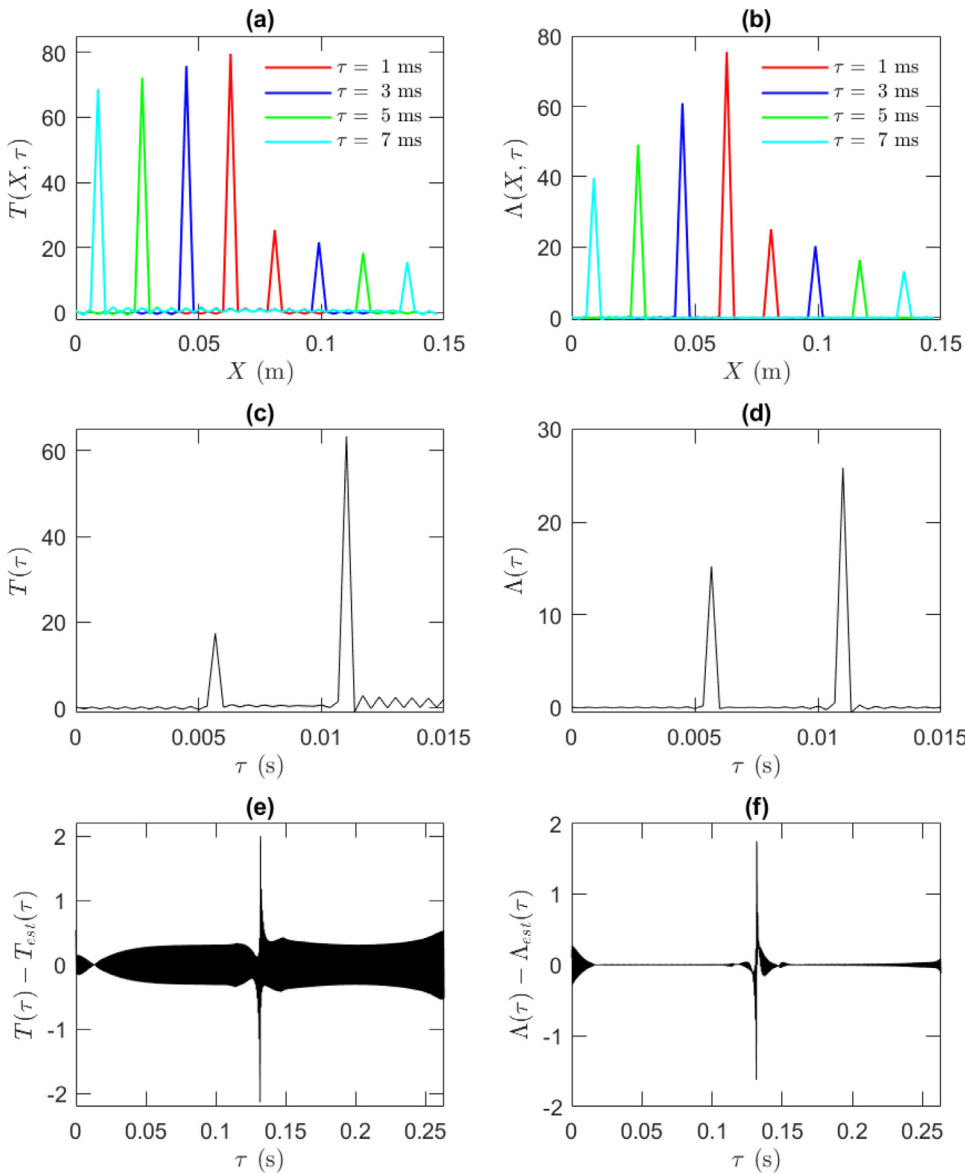


Fig. 4. The 1D asymmetric test case described by Eq. (60) with $\eta = -0.5$. (a) $T(X, \tau)$ (colored lines) for four time delays, corresponding to the response of the system to a delta function input at the central point. Note that these curves for T and T_{est} are almost indistinguishable on this scale; errors are discussed in the text. (b) As for (a), but plotting $\Lambda(\tau)$. (c) Example temporal evolution, $T(\tau)$, between points separated by 0.051 m. (d) As for (c), but $\Lambda(\tau)$. (e) $T(\tau) - T_{\text{est}}(\tau)$ for points separated by 0.051 m. (f) As for (e), but $\Lambda(\tau) - \Lambda_{\text{est}}(\tau)$.

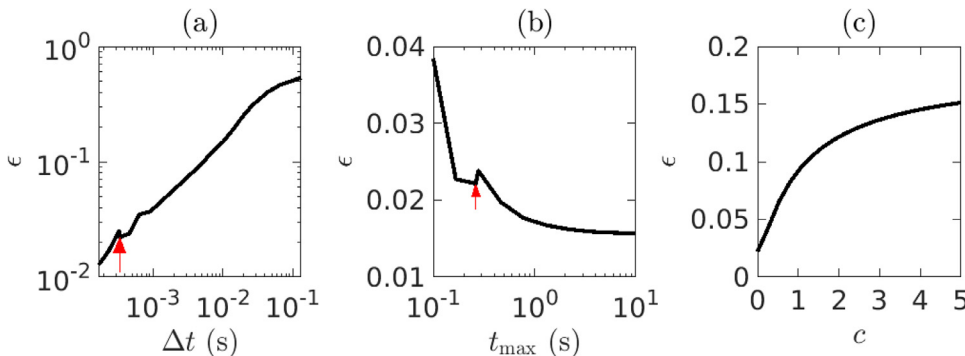


Fig. 5. Error ϵ in estimation of the 1D asymmetric test case described by Eq. (60) with $\eta = -0.5$. (a) ϵ vs. sampling interval Δt , with total sampling time $t_{\text{max}} = 0.26$ s. Nominal value is indicated by an arrow. (b) ϵ vs. t_{max} , with $\Delta t = 0.33$ ms. Nominal value is indicated by an arrow. (c) ϵ vs. noise level c with $\Delta t = 0.33$ ms and $t_{\text{max}} = 0.26$ s.

temporal resolution is not needed. Incidentally, these spatial scales and frequency ranges are well within the capabilities of high-resolution EEG, but not functional MRI.

In the 1D case the largest errors in $T_{\text{est}}(\tau)$ were around $t_{\text{max}}/2$. Here we aim to demonstrate an accurate estimate of T , including around $t_{\text{max}}/2$ and therefore choose $t_{\text{max}} = 10$ s, which is large. If only shorter time T_{est} responses are needed, then t_{max} can be reduced at the cost of

somewhat increased error in that range, but reduced runtime. The above choices give $n_t = 1624$ and $\Delta f = 0.1$ Hz.

Using the above parameters, Fig. 6 shows the outward propagation of the response to a delta function input at the central point of the system for time delays of 10 ms, 20 ms, and 30 ms, illustrating the dynamics of $T(\tau)$, $\Lambda(\tau)$, and $\Gamma(\tau)$. Fig. 7 shows the full temporal extent of $T(\tau)$, $\Lambda(\tau)$, and $\Gamma(\tau)$, and differences from their estimated quantities for points sepa-

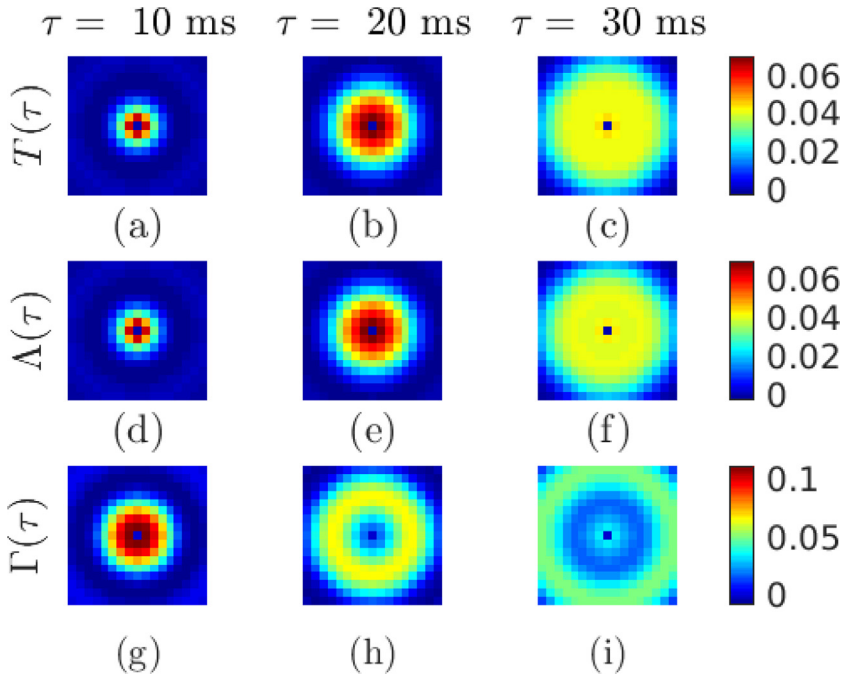


Fig. 6. 2D test case described by Eqs (64) and (66). The system is approximately discretized into a 17×17 grid of equally spaced points of side length 47 cm, with periodic boundaries, over a frequency range of 0 to 162 Hz in 0.1 Hz increments. Each frame shows the spatial response to a delta function input at the central point, with time delays since input of 10 ms, 20 ms and 30 ms from left to right. In all frames the differences between the actual and estimated quantities are imperceptible at the scales shown. (a)-(c) $T(\tau)$. (d)-(f) $\Lambda(\tau)$. (g)-(i) $\Gamma(\tau)$.

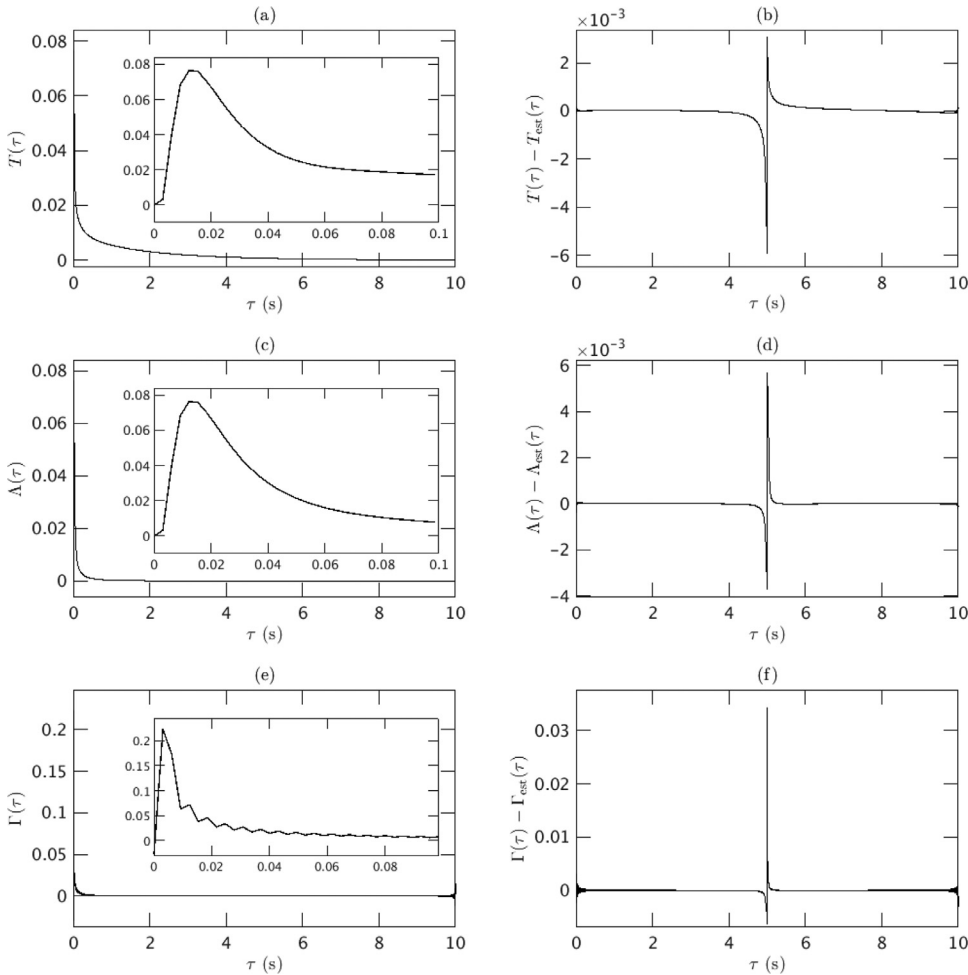


Fig. 7. 2D test case described by Eqs (64) and (66). The system is approximately discretized into a 17×17 grid of equally spaced points of side length 47 cm, with periodic boundaries, over a frequency range of 0 to 162 Hz in 0.1 Hz increments. Plots are for T , Λ , and Γ between points separated by half the grid dimension, 23.5 cm. Insets enlarge parts of curves not well resolved in the full frames. (a) $T(\tau)$. (b) $T(\tau) - T_{est}(\tau)$. (c) $\Lambda(\tau)$. (d) $\Lambda(\tau) - \Lambda_{est}(\tau)$. (e) $\Gamma(\tau)$. (f) $\Gamma(\tau) - \Gamma_{est}(\tau)$.

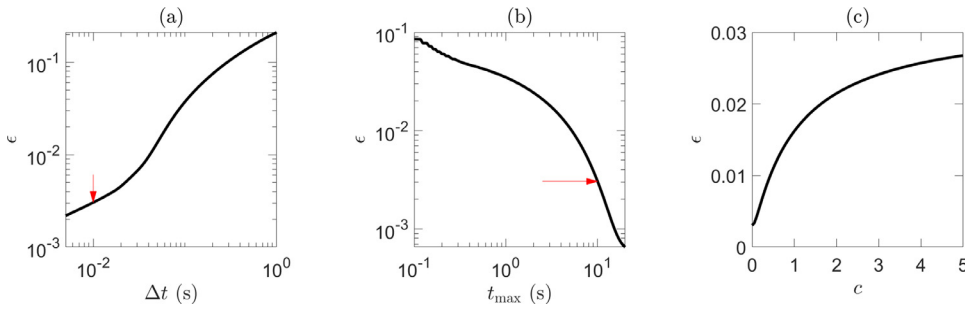


Fig. 8. Errors in estimation of the 2D transfer function described by Eqs (64) and (66). Nominal value is indicated by an arrow. (a) ϵ vs. Δt , with $t_s = 10$ s. (b) ϵ vs. t_{\max} , with $\Delta t = 1.67$ ms. (c) ϵ vs. noise level c , with $t_{\max} = 10$ s and $\Delta t = 1.67$ ms. (d) ϵ vs. Δx , with $t_{\max} = 10$ s and $\Delta t = \Delta x/v$.

rated by half the grid dimension, 23.5 cm. From these figures, we can see that T and Λ are very similar for the first few tens of milliseconds, where T is dominated by direct propagation in Λ ; however, as τ increases, so to does indirect propagation and T decays more slowly than Λ . Numerical results (not shown) demonstrate that this difference becomes more noticeable in cases in which the system is closer to criticality.

During the initial response ($\tau \lesssim 5$ s), the peak difference in $T(\tau) - T_{\text{est}}(\tau)$ is almost three orders of magnitude smaller than the peak value of $T(\tau)$, and $\epsilon = 0.002$. In Fig. 7(a), we can see that T has decayed almost to zero at $\tau = 10$ s and so $t_{\max} = 10$ s has captured most of the slow dynamics. We see in Figs 7(b), (d), and (f) that the central artifact at $t_{\max}/2$ remains, as in the 1D case; however, most of the system response has been captured and the error is much smaller. Since the algorithm produces an artifact centered on $t_{\max}/2$, to avoid this artifact t_{\max} should be chosen to be more than twice the maximum desired time response, as in Eq. (58).

Dependence of Accuracy on Sampling Parameters Fig. 8 shows how ϵ depends on sampling parameters Δt and t_{\max} . We use a coarser 11×11 grid of 121 points than in Section 3.3.2 to reduce computational resource requirements, giving $n_x = 11$ and $\Delta x = 42.7$ mm. In Fig. 8(a) t_{\max} is fixed at 10 s, and the red arrow indicates the point corresponding to $\Delta t = 10$ ms as used in Section 3.3.2. As Δt increases, the fast dynamics of the system are increasingly missed, so ϵ increases. Fig. 8(b) shows ϵ vs. t_{\max} for Δt fixed at 10 ms. The red arrow indicates the point corresponding to $t_{\max} = 10$ s as used in Section 3.3.2. We see that as t_{\max} increases, ϵ decreases due to the reduction of the artifact at $t_{\max}/2$, as well as error elsewhere. As t_{\max} is reduced, the position of the $t_{\max}/2$ artifact is shifted closer to the large initial response, the size of the artifact increases and it occupies a larger fraction of the range of $T(\tau)$, thus increasing ϵ .

Fig. 8 (b) shows how ϵ depends on t_{\max} . As Fig. 7 showed, most of the response for the 2D system is concentrated very close to 0 Hz. As t_{\max} decreases, the frequency resolution is coarser and the slow dynamics of the system are less well represented, so ϵ increases significantly. Thus, when t_{\max} is large, ϵ is small; here $\epsilon = 0.004$ when $t_{\max} = 10$ s.

Dependence of Accuracy on Noise As for the 1D test case, Fig. 8(c) shows ϵ with the addition of white, additive measurement noise using Eq. (63). When $c = 0$, there is no noise and $\epsilon \approx 0.004$ is small. As c increases, the error rises quickly, until about $c \approx 1$ when the measurement noise has the same strength as the input noise. As c increases further, the $c^2 I$ term in Eq. (63) dominates and $T_{\text{est}} \rightarrow I$ and little information about the underlying system is recovered. Overall, the error is much smaller than in the 1D test case in Fig. 5(c) because from Eq. (63), adding noise forces T_{est} to be closer to I , but in this 2D system high frequencies are filtered out, so T is already close to I at high frequencies.

Numerical Runtime We find that the code runs on a PC in a reasonable time for problems of a size that is of the same order as those encountered in typical experimental situations. For example, a case with $M = 100$ and $n_t = 1000$ takes around 40 s on a single-core of an Intel Xeon E5-2697 V4 CPU with base clock speed of 2.6 GHz. Exploration of a number of different values verified the n_t dependence in Eq. (50) and did not find any additional M dependence of the number of iterations required to converge to a specified accuracy, although the dependence on M was

still approaching its asymptotic form from above. Hence, we estimate a runtime of

$$T \approx 4 \times 10^{-8} n_t M^3 \text{ s}, \quad (67)$$

for this machine; however, the 4×10^{-8} constant is an overestimate of the actual value because the asymptotic form was not reached and converges from above.

3.3.3. Transfer function estimation for NFT on a discrete network with complex anatomical connectivity

Understanding the relationships between brain activity and its underlying physiology and connectivity is a central problem in neuroscience and many other real world systems of interest have complex connectivity structure; thus we next test the Wilson algorithm for systems with a complex connectivity, or network architecture, and brain-like dynamics at the nodes.

Estimation of Connection Matrix-Based Transfer Function A population averaged anatomical cortical connectivity dataset (Yeh et al., 2018) is used as the basis for calculations in this section. This dataset is derived from diffusion MRI of 824 healthy subjects in the Human Connectome Project database (Essen et al., 2012), discretized into 400 regions distributed across both cortical hemispheres (Schaefer et al., 2018). The anatomical connection strengths in this dataset are based on white matter fiber counts of axons connecting regions pairwise and do not include local connections within a region, inhibitory connections, nor any information on directionality. Overall, the matrix of detected connections is sparse, meaning that many connections were undetected or absent, and connections that were detected vary in strength over three orders of magnitude, so it is essential to determine whether the algorithm can accurately reconstruct the transfer function given these complexities. For demonstration purposes, we restrict attention to the left hemisphere, in which 172 regions out of 200 were found to be connected to at least one other region; others were removed from the dataset before proceeding. We stress that we are not concerned with the validity of this dataset as regards state of the art connectivity estimation, only to provide an example of a large and extremely complicated connectivity dataset for test purposes.

Having been obtained by diffusion MRI, the dataset does not contain information on time delays for signals to propagate between regions; nor does it contain information on the absolute strength of connections. So for demonstration purposes, we assume that signals propagate between points separated by a Euclidean distance r according to the NFT propagator in Eq. (66), which implies relevant time delays and dispersion and G is taken to be the strength of connectivity in the dataset. We also multiply the connectivity strengths by a factor such that the largest eigenvalue of Λ is $\lambda_1 = 0.85$ to ensure that the system is stable but near criticality. If spectral factorization is used to obtain T_{est} , then the structural connectivity can be further estimated by rearranging rearranging (14) and assuming NFT dynamics in (64)-(66) to find G .

In choosing sampling parameters, we note that the smallest Euclidean separation of regions is $\Delta x = 6.9$ mm which implies $\Delta t = 0.8$ ms and $f_{\max} = 650$ Hz using Eqs (52) and (55), while the typical separation

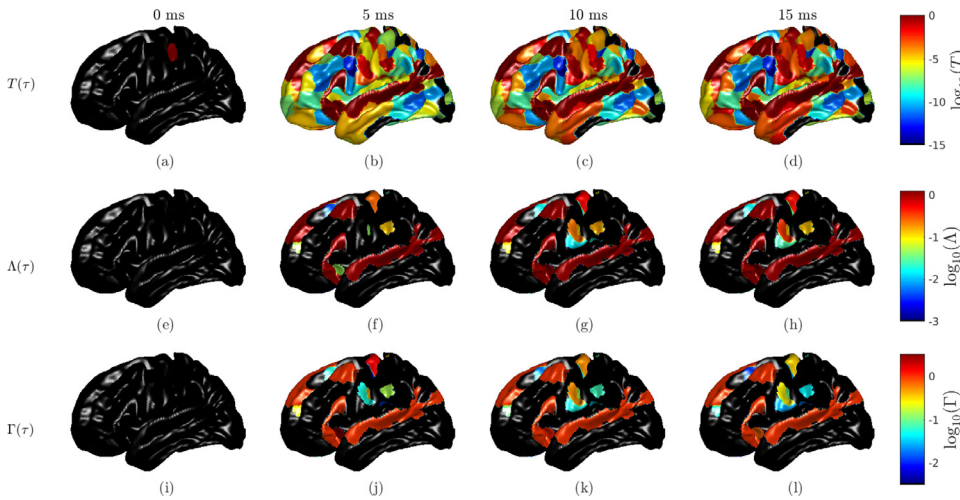


Fig. 9. Test case using anatomical connectivity combined with the 2D NFT propagator described by Eqs (66) and (64). The system is composed of the left hemisphere only, with 201 ROIs, only 172 have connections to other ROIs. Disconnected ROIs are black. Activity is stimulated in one ROI and plotted for four time-points from the application of the stimulus. The differences between T and T_{est} are imperceptible at the scales shown. (a) $T(\tau = 0 \text{ ms})$, showing the stimulated ROI in red. (b) $T(\tau = 5 \text{ ms})$. (c) $T(\tau = 10 \text{ ms})$. (d) $T(\tau = 15 \text{ ms})$. (e) $\Lambda(\tau = 0 \text{ ms})$. (f) $\Lambda(\tau = 5 \text{ ms})$. (g) $\Lambda(\tau = 10 \text{ ms})$. (h) $\Lambda(\tau = 15 \text{ ms})$. (i) $\Gamma(\tau = 0 \text{ ms})$. (j) $\Gamma(\tau = 5 \text{ ms})$. (k) $\Gamma(\tau = 10 \text{ ms})$. (l) $\Gamma(\tau = 15 \text{ ms})$.

is around 30 mm, which corresponds to $\Delta t = 3.3 \text{ ms}$ and $f_{\text{max}} = 150 \text{ Hz}$. However, as described in Section 3.3.2, dendritic and soma dynamics described by Eq. (65) act as a low pass filter, limiting large-scale dynamics to $f \lesssim 50 \text{ Hz}$. Here we choose $f_{\text{max}} = 150 \text{ Hz}$ so $\Delta t = 5 \text{ ms}$ and $\Delta x = 30 \text{ mm}$. The presence of many very weak, or absent connections in the dataset means that indirect propagation of activity tends to be reduced in comparison to the uniform 2D case in Section 3.3.2. This means that the decay of T tends to more closely match that of Λ than in the 2D case, allowing the slow system dynamics to be captured by a smaller t_{max} . We therefore choose $t_{\text{max}} = 5 \text{ s}$ ($\Delta f = 0.2 \text{ Hz}$); however, as in the other test cases, smaller t_{max} can be chosen at the cost of increased error in that range, but reduced runtime.

Fig. 9 shows four snapshots of $T(\tau)$, $\Lambda(\tau)$ and $\Gamma(\tau)$, to a delta function input to the single discretized region shown in red in Fig. 9(a), plotted on the surface of a left hemisphere. Few areas display significant activity because the measured connectivity is sparse and often very weak; however, activity does spread to other ROIs. Over the plotted timescale, responses tend to increase over time with some ROI responses increasing by many orders of magnitude. As described above, because most connections are weak, elements of T and Λ tend to be similar; however, Γ does not contain the low pass filtering of \mathcal{L} and so activity can be seen in Γ sooner than in Λ and T .

Fig. 10 shows one representative element of $T(\tau)$, $\Lambda(\tau)$ and $\Gamma(\tau)$ and differences $T(\tau) - T_{\text{est}}(\tau)$, $\Lambda(\tau) - \Lambda_{\text{est}}(\tau)$ and $\Gamma(\tau) - \Gamma_{\text{est}}(\tau)$. The difference between $T(\tau)$ and $T_{\text{est}}(\tau)$ is small with $\epsilon = 0.0011$, and is especially small away from the $t_{\text{max}}/2$ artifact, meaning that the Wilson algorithm is able to closely estimate T for systems with brain-like dynamics and complex connectivity and, more generally, systems with complex network architectures and time delays.

As described above, the faster appearance of a response in Γ than in Λ and T can be seen by comparing Fig. 10(e) to Fig. 10(a) and (c), as can the similarity of T and Λ owing to the many weak or absent connections producing a highly nonuniform system, reducing indirect propagation of activity along many pathways in comparison to the uniform 2D case in Section 3.3.2. These indirect paths can be very long, and thus contribute to slower responses. Note that because activity can be propagated via very many indirect pathways that involve weak connections, it is important for experiments measuring structural connectivity to capture all connections, including weak ones and not remove them via thresholding. However, we reiterate that our aim here is only to demonstrate that the algorithm can handle systems of similar complexity to those observed in brains.

Often brain connectivity data are presented in the form of a connection matrix (CM) (Brown et al., 2012). This is especially common for functional connectivity data defined to be two-point covariances,

$C(\tau = 0)$, of fMRI time series. However, the dynamics of a system cannot practically be inferred from visual plots of correlations. In contrast, T provides direct information about the dynamical influence of ROIs on one another. Because T is the impulse response of the system, it is also much more useful than C for incorporating into further analysis and modeling, as described in Section 2. Fig. 11 shows $T(\tau)$ in connection matrix (CM) format, with each column showing how activity spreads from a delta function input at the ROI corresponding to that column, as shown in Fig. 9. The mapping of the 2D cortical surface onto a 1D set of matrix indices means that patterns in the CMs are difficult to interpret visually and much of the apparent structure is an artifact of that mapping (Henderson and Robinson, 2011, 2013, 2014); however, entries near the diagonal tend to be for nearby ROIs. Thus, strong initial responses in Fig. 11(c) and (d) tend to be clustered around the diagonals, but it should be noted from (g), that even after only 20 ms the response has spread widely in the system and the lowest eigenmodes dominate over the short-scale ones that are only excited for a short period after an initial δ input (Mukta et al., 2019; 2020). After 1 s, shown in (h), the response is widely spread, and the initial large responses have been attenuated greatly by damping. These temporally changing patterns of network dynamics provide a promising approach to understanding the dynamic functional connectivity patterns in fMRI CMs (Hansen et al., 2015), providing a much more informative picture of the static structural and functional connectivities in Fig. 11(a) and (e), respectively.

4. Discussion and conclusion

The present work emphasizes the importance of the brain's linear transfer function in describing and analyzing brain structure and function. The main results are:

(i) We stressed and illustrated how the linear transfer function of a system contains complete information about its linear properties, responses, and dynamics, and interrelates a wide range of commonly used brain measures and analyses. The transfer function is central to a systematic, self-consistent description of brain anatomy, physiology and dynamics which connect brain structure to brain function. These relations were described in continuous coordinate notation, reflecting the continuous underlying brain system at the scales of interest, as well as in discrete matrix form that is easily applicable to inherently discrete experimental measurements that probe the underlying continuum.

(ii) It was shown that the transfer function can be efficiently obtained via spectral methods using evoked potentials or correlation functions. We focused on the Wilson factorization algorithm applied to correlation matrices.

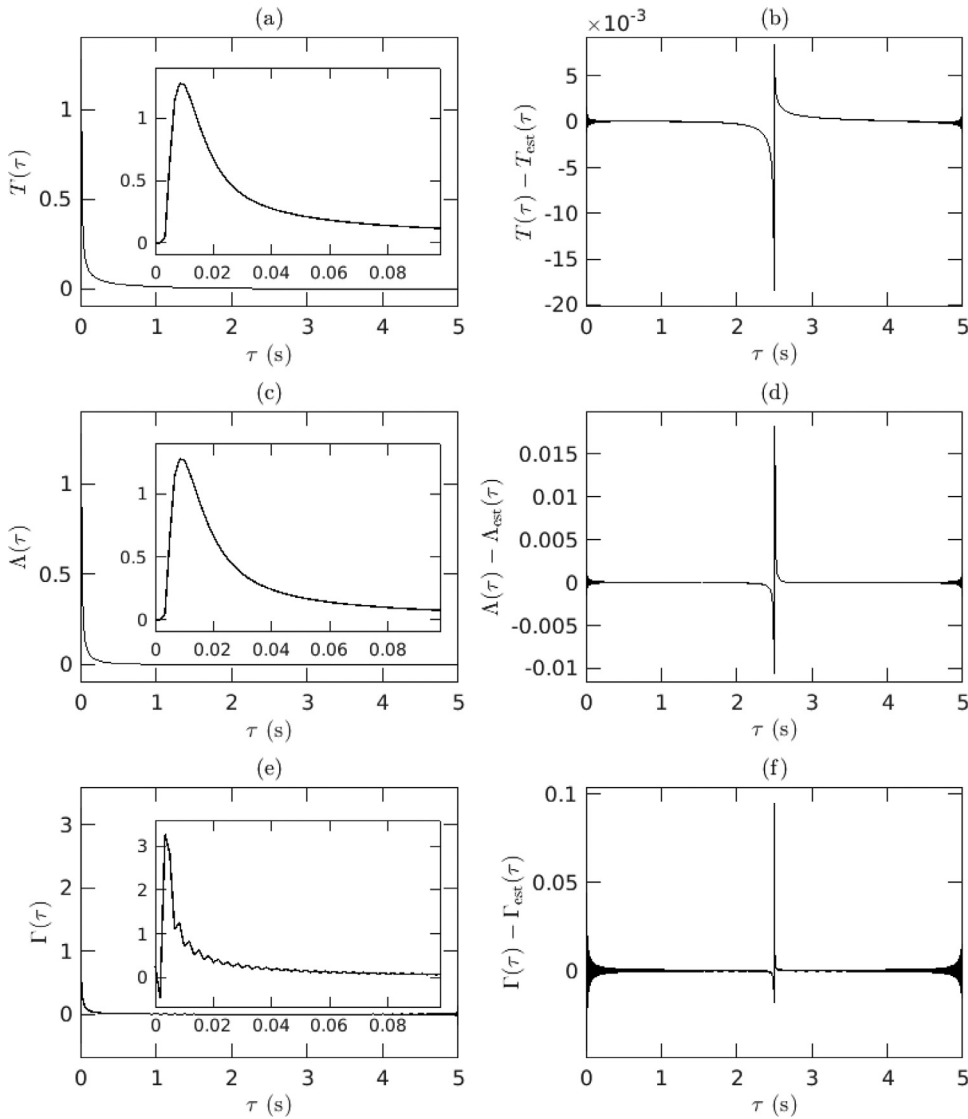


Fig. 10. Test case using anatomical connectivity combined with the 2D NFT propagator described by Eqs (66) and (64). Insets enlarge parts of curves not well resolved in the full frames. (a) $T(\tau)$. (b) $T(\tau) - T_{\text{est}}(\tau)$. (c) $\Lambda(\tau)$. (d) $\Lambda(\tau) - \Lambda_{\text{est}}(\tau)$. (e) $\Gamma(\tau)$. (f) $\Gamma(\tau) - \Gamma_{\text{est}}(\tau)$.

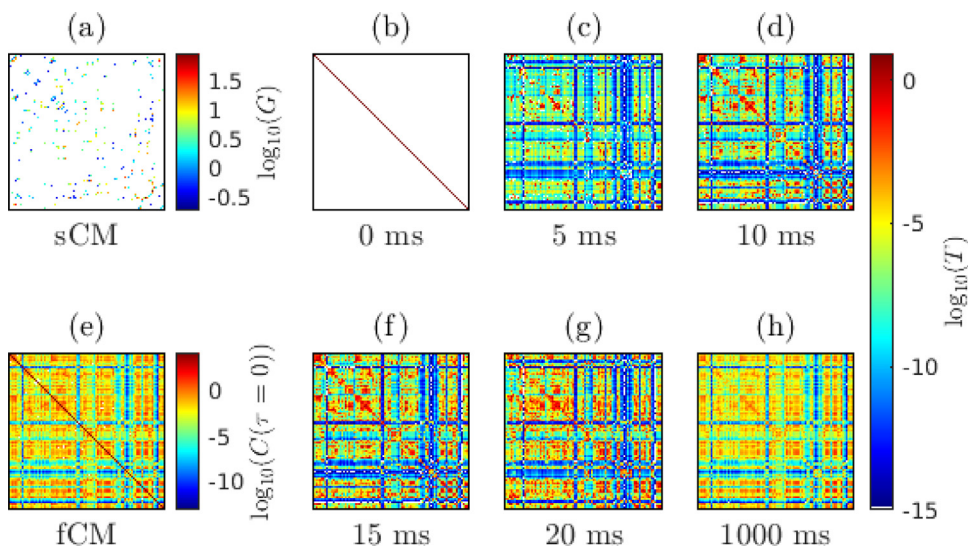


Fig. 11. Test case using anatomical connectivity combined with the 2D NFT propagator described by Eqs (66) and (64). The system is composed of the 172 connected ROIs in the left hemisphere only. Plots are in connection matrix format, white indicates zero entries. (a) Anatomical connectivity strength used for G . (b) $T(\tau = 0 \text{ ms})$, showing the input to each ROI along the diagonal. (c) $T(\tau = 5 \text{ ms})$. (d) $T(\tau = 10 \text{ ms})$. (e) Functional connectivity, $C(\tau = 0)$. (f) $T(\tau = 15 \text{ ms})$. (g) $T(\tau = 20 \text{ ms})$. (h) $T(\tau = 1000 \text{ ms})$.

(iii) We have provided MatLab code (<https://github.com/BrainDynamicsUSYD/SpecFac>) that implements the Wilson spectral factorization algorithm and have showed that its runtime is practical for systems of hundreds of elements, as in MEG experiments and high-density EEG recordings, for example.

(iv) We provide criteria for sampling time series in experiments, and test the performance of the Wilson algorithm with variation in these parameters. Measurement times of a few seconds or longer provide an accurate estimate of the transfer function for brain-like dynamics; however, measurement times can be reduced if the focus is on short-time dynamics, thereby reducing runtimes commensurately. We show that the algorithm produces its largest error in the estimated transfer function at the midpoint of its temporal range, and that the size of the error is reduced by increasing the duration and temporal resolution of the measured time series used in constructing the cross spectrum input to the algorithm. For long, high frequency time series recordings, the error can be made negligible.

In practice the ground truth is not known to be able to infer the quality of the estimated transfer function for a given set of measurement parameters. However, convergence of the algorithm's estimate of the transfer function toward the limit of infinitely fine sampling resolution can be inferred by varying the measurement parameters and observing the change in the resulting estimated transfer function; extrapolating these changes can also be considered. A suitable set of measurement parameters should be indicated when the change to the estimated transfer function is small.

These measurement criteria obtained imply that experimental modalities like EEG and MEG are suitable for determining time delays, but with EEG having relatively coarse spatial resolution. fMRI cannot be used to determine neural level time delays because of its maximum sampling rate of only a few Hz and the intrinsically slow (~ 1 s timescale) hemodynamic response that underlies it (Chen et al. (2019); Demetriou et al. (2018)). However, we introduced a modal projection that makes use of fMRI's high spatial resolution to obtain the spatial structure of eigenmodes. The spatial component of the eigenmodes was then combined with the temporal structure of a transfer function obtained via spectral factorization of high temporal resolution EEG or MEG time series data. By combining fMRI, and EEG or MEG it is possible to obtain low order modes of a brain transfer function with both high spatial and temporal resolution which can help with properly interpreting and understanding observations of resting state networks and default mode networks, for example.

(v) The Wilson algorithm was demonstrated to accurately estimate known transfer functions constructed in successively more realistic and complicated test cases derived from neural field theory. These included systems containing delta function dynamics, systems with brain-like time delays in activity propagation, two dimensional systems, and systems with brain-like dynamics on complex discrete network architecture.

(vi) The performance of the algorithm was tested in the presence of additive white measurement noise. It was found that the error in the algorithm's output transfer function estimate was small provided that the strength of the noise was small relative to the system's actual input.

The performance of the algorithm for spectral Granger causality estimates with additive (independent and mixed) white noise in data has previously been assessed and found to be reasonably robust for noise amounts lower than signal levels (Pagnotta et al., 2018a,b). The use of time reversal testing was found to further mitigate the effects of noise (Winkler et al., 2016).

(vii) This good performance for a range of dynamical features provides confidence in the use of the algorithm on real data, and other non-neural systems. However, time series measurements include the underlying dynamics that are of interest, but also measurement dynamics and noise introduced via the measurement process. The details of noise and artefact components are specific to each modality and developing methods for filtering noise and artefacts from brain data is an active area

of research. Methods for removal of unwanted components of the transfer function can be applied to the measured time series, before being input to the algorithm; e.g., via source localization, or deconvolutional methods.

From these insights, it is clear that spectral factorization is a process that enables proper analysis of brain time series measurements; transforming functional CMs into transfer functions that provide a much more informative, dynamic perspective of the brain and enabling the use of a plethora of systematic analyses, as described in Sec 2.

Credit authorship contribution statement

James A. Henderson: Conceptualization, Methodology, Software, Formal analysis, Writing - original draft, Writing - review & editing. **Mukesh Dhamala:** Conceptualization, Methodology, Software, Writing - review & editing. **Peter A. Robinson:** Conceptualization, Methodology, Supervision, Funding acquisition, Writing - original draft, Writing - review & editing.

Acknowledgments

We thank L. Ephremidze for stimulating discussions. This work was supported by the Australian Research Council under Center of Excellence grant CE14010007 and Laureate Fellowship grant FL140100025.

Supplementary material

Supplementary material associated with this article can be found, in the online version, at [10.1016/j.neuroimage.2021.117989](https://doi.org/10.1016/j.neuroimage.2021.117989)

References

- Abeysuriya, R.G., Rennie, C.J., Robinson, P.A., 2014. Prediction and verification of non-linear sleep spindle harmonic oscillations. *J. Theor. Biol.* 344, 70.
- Abeysuriya, R.G., Rennie, C.J., Robinson, P.A., 2015. Physiologically based arousal state estimation and dynamics. *J. Neurosci. Meth.* 253, 55.
- Abeysuriya, R.G., Robinson, P.A., 2016. Real-time automated EEG tracking of brain states using neural field theory. *J. Neurosci. Methods* 258, 28.
- van Albada, S.J., Kerr, C.C., Chiang, A.K.I., Rennie, C.J., Robinson, P.A., 2010. Neurophysiological changes with age probed by inverse modeling of EEG spectra. *Clin. Neurophysiol.* 121, 21.
- van Albada, S.J., Rennie, C.J., Robinson, P.A., 2007. Variability of model-free and model-based quantitative measures of EEG. *J. Int. Neurosci.* 06, 279.
- Babaie-Janvier, T., Robinson, P.A., 2018. Neural field theory of corticothalamic prediction with control systems analysis. *Front. Hum. Neurosci.* 12, 334.
- Breakspear, M., Heitmann, S., Daffertshofer, A., 2010. Generative models of cortical oscillations: neurobiological implications of the Kuramoto model. *Front. Hum. Neurosci.* 4, 190.
- Brown, J., Rudie, J., Bandrowski, A., Horn, J.V., Bookheimer, S., 2012. The UCLA multimodal connectivity database: a web-based platform for brain connectivity matrix sharing and analysis. *Front. Neuroinf.* 6, 28.
- Chen, J.E., Polimeni, J.R., Bollmann, S., Glover, G.H., 2019. On the analysis of rapidly sampled fMRI data. *Neuroimage* 188, 807.
- Coppersmith, D., Winograd, S., 1990. Matrix multiplication via arithmetic progressions. *J. Symbolic Comput.* 9, 251.
- Deco, G., Jirsa, V.K., Robinson, P.A., Breakspear, M., Friston, K., 2008. The dynamic brain: from spiking neurons to neural masses and cortical fields. *PLoS Comput. Biol.* 4, 1.
- Demetriou, L., Kowalczyk, O.S., Tyson, G., Bello, T., Newbould, R.D., Wall, M.B., 2018. A comprehensive evaluation of increasing temporal resolution with multiband accelerated protocols and effects on statistical outcome measures in fMRI. *Neuroimage* 176, 404.
- Dhamala, M., Rangarajan, G., Ding, M., 2008. Estimating Granger causality from Fourier and wavelet transforms of time series data. *Phys. Rev. Lett.* 100, 018701.
- Dhamala, M., Rangarajan, G., Ding, M., 2008. Analyzing information flow in brain networks with nonparametric Granger causality. *Neuroimage* 41, 354.
- Ephremidze, L., Janashia, G., Lagvilava, E., 2008. An analytic proof of the matrix spectral factorization theorem. *Georgian Math. J.* 15, 241–249.
- Ephremidze, L., Saied, F., Spitkovsky, I.M., 2018. On the algorithmization of Janashia-Lagvilava matrix spectral factorization method. *IEEE Trans. Inf. Theory* 64, 1369.
- Essen, D.V., Ugurbil, K., Auerbach, E., Barch, D., Behrens, T.E.J., Bucholz, R., Chang, A., Chen, L., Corbetta, M., Curtiss, S.W., Penna, S.D., Feinberg, D., Glasser, M.F., Harel, N., Heath, A.C., Larson-Prior, L., Marcus, D., Michalareas, G., Moeller, S., Oostenveld, R., Petersen, S.E., Prior, F., Schlaggar, B.L., Smith, S.M., Snyder, A.Z., Xu, J., Yacoub, E., 2012. The human connectome project: a data acquisition perspective. *Neuroimage* 62, 2222.

- Fox, M.D., Snyder, A.Z., Zacks, J.M., Raichle, M.E., 2006. Coherent spontaneous activity accounts for trial-to-trial variability in human evoked brain responses. *Nat. Neurosci.* 9, 23.
- Friston, K.J., Bastos, A.M., Oswal, A., van Wijk, B., Richter, C., Litvak, V., 2014. Granger causality revisited. *Neuroimage* 101, 796.
- Gabay, N.C., Babaie-Janvier, T., Robinson, P.A., 2018. Dynamics of cortical activity eigenmodes including standing, traveling, and rotating waves. *Phys. Rev. E* 98, 042413.
- Gabay, N.C., Robinson, P.A., 2017. Cortical geometry as a determinant of brain activity eigenmodes: neural field analysis. *Phys. Rev. E* 96, 032413.
- Hansen, E.C., Battaglia, D., Spiegler, A., Deco, G., Jirsa, V.K., 2015. Functional connectivity dynamics: modeling the switching behavior of the resting state. *Neuroimage* 105, 525.
- Henderson, J.A., Robinson, P.A., 2011. Geometric effects on complex network structure in the cortex. *Phys. Rev. Lett.* 107, 018102.
- Henderson, J.A., Robinson, P.A., 2013. Using geometry to uncover relationships between isotropy, homogeneity, and modularity in cortical connectivity. *Brain Connect.* 3, 423.
- Henderson, J.A., Robinson, P.A., 2014. Relations between the geometry of cortical gyrification and white-matter network architecture. *Brain Connect.* 4, 112.
- Horn, R.A., Johnson, C.R., 2013. *Matrix analysis*, 2nd ed. Cambridge University Press, New York.
- Kahn, I., Desai, M., Knoblich, U., Bernstein, J., Henninger, M., Graybiel, A.M., Boyden, E.S., Buckner, R.L., Moore, C.I., 2011. Characterization of the functional MRI response temporal linearity via optical control of neocortical pyramidal neurons. *J. Neurosci.* 31, 15086.
- Kandel, E.R., Schwartz, J.H., Jessell, T.M., Siegelbaum, S.A., Hudspeth, A.J., 2012. *Principles of neural science*, 5th ed. McGraw-Hill Education, New York.
- Kerr, C.C., Rennie, C.J., Robinson, P.A., 2008. Physiology based modeling of cortical auditory evoked potentials. *Biol. Cybern.* 98, 171.
- Kerr, C.C., Rennie, C.J., Robinson, P.A., 2011. Model based analysis and quantification of age trends in auditory evoked potentials. *Clin. Neurophysiol.* 122 (134), 1336.
- Liu, T.T., Nalci, A., Falahpour, M., 2017. The global signal in fMRI: nuisance or information? *Neuroimage* 150, 213.
- Logothetis, N.K., Pauls, J., Augath, M., Trinath, T., Oeltermann, A., 2001. Neurophysiological investigation of the basis of the fMRI signal. *Nature* 412, 150.
- Luck, S.J., Kappenman, E.S., 2012. *The Oxford handbook of event-related potential components*. Oxford University Press, Oxford.
- MacLaurin, J.N., Robinson, P.A., 2019. Determination of effective brain connectivity from activity correlations. *Phys. Rev. E* 99, 042404.
- Markov, N.T., Ercsey-Ravasz, M.M., Gomes, A.R.R., Lamy, C., Magrou, L., Vezoli, J., Misery, P., Falchier, A., Quilodran, R., Gariel, M.A., Sallet, J., Gamanut, R., Huissoud, C., Clavagnier, S., Giroud, P., Sappey-Mariniere, D., Barone, P., Dehay, C., Toroczkai, Z., Knoblauch, K., Essen, D.C.V., Kennedy, H., 2012. A weighted and directed interareal connectivity matrix for macaque cerebral cortex. *Cereb. Cortex* 24, 17.
- Mehta-Pandjee, G., Robinson, P.A., Henderson, J.A., Aquino, K.M., Sarkar, S., 2017. Inference of direct and multistep effective connectivities from functional connectivity of the brain and of relationships to cortical geometry. *J. Neurosci. Methods* 283, 42.
- Mukta, K.N., Gao, X., Robinson, P.A., 2019. Neural field theory of evoked response potentials in a spherical brain geometry. *Phys. Rev. E* 99, 062304.
- Mukta, K.N., Robinson, P.A., Pagès, J.C., Gabay, N.C., Gao, X., 2020. Evoked response activity eigenmode analysis in a convoluted cortex via neural field theory. *Phys. Rev. E* 102, 062303.
- Norcia, A.M., Appelbaum, L.G., Ales, J.M., Cottareau, B.R., Rossion, B., 2015. The steady-state visual evoked potential in vision research: a review. *J. Vis.* 15, 1.
- Nunez, P.L., 1995. *Neocortical dynamics and human EEG rhythms*. Oxford University Press, Oxford.
- Pagnotta, M.F., Dhamala, M., Plomp, G., 2018. Assessing the performance of Granger-Geweke causality: benchmark dataset and simulation framework. *Data Brief* 21, 833.
- Pagnotta, M.F., Dhamala, M., Plomp, G., 2018. Benchmarking nonparametric Granger causality: robustness against downsampling and influence of spectral decomposition parameters. *Neuroimage* 183, 478.
- Robinson, P.A., 2012. Interrelating anatomical, effective, and functional brain connectivity using propagators and neural field theory. *Phys. Rev. E* 85, 011912.
- Robinson, P.A., 2013. Discrete-network versus modal representations of brain activity: why a sparse regions-of-interest approach can work for analysis of continuous dynamics. *Phys. Rev. E* 88, 054702.
- Robinson, P.A., 2019. Physical brain connectomics. *Phys. Rev. E* 99, 012421.
- Robinson, P.A., Rennie, C.J., Rowe, D.L., 2002. Dynamics of large-scale brain activity in normal arousal states and epileptic seizures. *Phys. Rev. E* 65, 041924.
- Robinson, P.A., Rennie, C.J., Wright, J.J., 1997. Propagation and stability of waves of electrical activity in the cerebral cortex. *Phys. Rev. E* 56, 826.
- Robinson, P.A., Sarkar, S., Pandjee, G.M., Henderson, J.A., 2014. Determination of effective brain connectivity from functional connectivity with application to resting state connectivities. *Phys. Rev. E* 90, 012707.
- Robinson, P.A., Zhao, X., Aquino, K.M., Griffiths, J.D., Sarkar, S., Mehta-Pandjee, G., 2016. Eigenmodes of brain activity: neural field theory predictions and comparison with experiment. *Neuroimage* 142.
- Scannell, J.W., Blakemore, C., Young, M.P., 1995. Analysis of connectivity in the cat cerebral cortex. *J. Neurosci.* 15, 1463.
- Schaefer, A., Kong, R., Gordon, E.M., Laumann, T.O., Zuo, X.N., Holmes, A.J., Eickhoff, S.B., Yeo, B.T.T., 2018. Local-global parcellation of the human cerebral cortex from intrinsic functional connectivity MRI. *Cereb. Cortex* 28, 3095.
- Silva, F.H.L.d., 2013. EEG and MEG: relevance to neuroscience. *Neuron* 80, 1112.
- Huang, J., Smith, T.M., Henry, G.M., 2016. R. A. van de Geijn. In: *SC '16: Proceedings of the International Conference for High Performance Computing, Networking, Storage and Analysis*, pp. 690–701.
- J.O., Smith III, 2007. *Introduction to Digital Filters with Audio Applications*.
- Strassen, V., 1969. Gaussian elimination is not optimal. *Numer. Math.* 13, 354.
- T. Wilson, G., 1972. The factorization of matricial spectral densities. *SIAM J. Appl. Math.* 23, 420.
- Winkler, I., Panknin, D., Bartz, D., Müller, K., Haufe, S., 2016. Validity of time reversal for testing Granger causality. *IEEE Trans. Signal Proc.* 64, 2746.
- Yeh, F.C., Panesar, S., Fernandes, D., Meola, A., Yoshino, M., Fernandez-Miranda, J.C., Vettel, J.M., Verstynen, T., 2018. Population-averaged atlas of the macroscale human structural connectome and its network topology. *Neuroimage* 178, 57.